GSA Data Repository 2019378 https://doi.org/10.1130/G46641.1

A true polar wander trigger for the great Jurassic East Asian Aridification

Zhiyu Yi[1]*, Yongqing Liu[1], Joseph G. Meert[2]

[1]Key Laboratory of Deep-Earth Dynamics of Ministry of Natural Resources, Institute of Geology, Chinese Academy of Geological Sciences, Beijing 100037, China.

[2]Department of Geological Sciences, 112 Williamson Hall, University of Florida, Gainesville, FL 32611, USA.

* To whom correspondence should be addressed.
Email: *yizhiyu09@gmail.com*

Supplementary Text

1. U-Pb Geochronology

Zircon grains were collected using standard crushing and mineral separation techniques. Zircons free of visible fractures or inclusions were handpicked under a binocular microscope. For U-Pb dating, zircons were mounted in an epoxy mount and were then polished to expose the half-sections for further analysis. Cathodoluminescence (CL) images were used to exam the structure of each zircon grain.

Selected zircons were subject to U-Pb dating by LA-ICP-MS at the Key Laboratory of Deep-Earth Dynamics of Ministry of Natural Resources, Institute of Geology, Chinese Academy of Geological Sciences. Detailed operating conditions for

the ICP-MS instrument, laser ablation system and data reduction process were described by Liu et al. (2010). A GeoLas 2005 was used for laser sampling. Ion-signal intensities were acquired using an Agilent 7500a ICPMS. A background acquisition of 20-30 seconds (gas blank) was conducted for each analysis, followed by data acquisition of 50 seconds from the sample. Each individual analysis was acquired using an Agilent Chemstation. Integration of background and analytical signals, off-line selection, time-drift correction and quantitative calibration for U-Pb dating were performed by ICP-MS-DataCal (Wiedenbeck et al., 1995). Zircon 91500 was measured twice every five analyses as the external standard for U-Pb dating. For every five analyses, a linear interpolation (with time) was used to correct the time-dependent drifts of U-Th-Pb isotopic ratios in accordance with the variations of 91500 (Liu et al., 2010; Wiedenbeck et al., 1995). Uncertainties of preferred values for the external standard 91500 were propagated through to obtain the ultimate results of the samples. Concordia diagrams and weighted average calculations were performed using Isoplot/Ex ver 2.4 to obtain the intercept and weighted mean ages (Ludwig, 2003).

In this study, most of the analyzed zircons from HW03 and HP14 are Jurassic in age and therefore yield low concentrations of ^{207}Pb relative to ^{206}Pb. Consequently, $^{206}Pb/^{207}Pb$ and $^{207}Pb/^{235}U$ ages have higher uncertainties than $^{206}Pb/^{238}U$ ages. $^{206}Pb/^{238}U$ ages were therefore used for the age interpretations. For older zircons, the $^{206}Pb/^{238}U$ age commonly underestimates actual age due to Pb loss, while $^{207}Pb/^{206}Pb$ age is closer to the primary crystallization age. Therefore, the $^{207}Pb/^{206}Pb$ age is adopted for zircons with $^{206}Pb/^{238}U$ ages >1000 Ma. In this study, $^{206}Pb/^{238}U$ ages are used for zircons with $^{207}Pb/^{206}Pb$ < 1000 Ma. Zircons with discordance > 10% were

discarded. The youngest zircon age populations were used to calculate the weighted mean age, which is interpreted to be the crystallization age.

2. Paleomagnetism

2.1 Methods

Standard cylindrical specimens were drilled in the field using a gasoline-powered drill. Generally, 10-12 paleomagnetic samples were collected from each site and all were collected using a portable gasoline-powered drill and oriented in situ by both magnetic and sun compasses.

Individual specimens were then cut and trimmed from the field samples. Specimens were subjected to stepwise thermal and alternating field (AF) demagnetization to determine the most effective procedure for isolating the ChRMs. Based on these trial specimens, most of the samples were subjected to progressive thermal demagnetization. A Schonstedt oven was used for thermal magnetization with residual magnetic field less than 10 nT inside the cooling chamber. Demagnetization was performed at 12-18 successive steps up to 580 ℃ or 685 ℃ degrees. Magnetic remanence was measured with a 2G 3-axis cryogenic magnetometer. All demagnetization and remanence measurements were performed in a magnetically shielded room at the laboratory of paleomagnetism at South China Sea Institute of Oceanology, Chinese Academy of Sciences.

Results were analyzed using principal component analysis of the vector components (Zijderveld, 1967; Kirschvink, 1980). Site mean directions were calculated using the characteristic remanent magnetizations (ChRMs) with maximum angular deviations (MADs) of less than 10°. Sample directions greater than two standard deviations away from the mean direction were excluded from the final mean. Site mean directions were calculated along with interval-mean results using standard

78 paleomagnetic statistical methods (Fisher, 1953). The uncertainty of paleolatitude is
79 determined by A_{95} of the paleopole.

80 ***2.2 Results***

81 Sites numbered from 'HW01' (top) to 'HW24' (bottom) were sampled in
82 stratigraphic order and represent multiple cooling units (Figs. DR1d and DR3). After
83 removing a viscous remanence by ~250 ℃, most specimens unblock between ~500 ℃
84 to 680 ℃ suggesting the existence of both magnetite and hematite. There is no
85 difference between the characteristic remanent magnetizations (ChRMs) carried by
86 magnetite and hematite (Fig. DR5a). A total of 213 out of 238 specimens yield
87 ChRMs that are statistically acceptable at site level. The 24 grouped site-mean
88 directions yield an interval-mean direction of D = 100.1 °, I = 59.9 ° (α_{95} = 7.8 °) before
89 and D = 21.9 °, I = 75.3 ° (α_{95} = 5.6 °) after tilt correction (Fig. 2B and Table DR3).
90 The other site (HW25), collected from a layer of breccia-bearing ignimbrite, yields
91 scattered ChRMs. An additional 3 sites were collected from sills intruding the
92 Nandaling Formation (Figs. DR3 and DR6b). The sills yield a mean direction of D =
93 44.9 °, I = 71.7 ° (α_{95} = 6.3 °) before and D = 352.9 °, I = 55.5 ° (α_{95} = 5.3 °) after tilt
94 correction (Table DR3).

95 A baked contact test was performed at site HW10 where samples were collected
96 along a profile from the chilled margin of an intruding dyke to the host rock (the
97 Nandaling Formation) (Fig. DR5b). The ChRMs obtained from the dyke and host
98 rocks unblocked at ~580 ℃ and ~680 ℃ respectively, suggesting that the magnetic
99 minerals of the two units are different (Fig. DR5b). The ChRMs of host rock samples
100 near the contact with the dyke (<20 cm distance) (Component A of HW10-20, 21, 22)
101 are statistically similar to those in the dyke (HW10-15, 16, 17, 18, 19) (Fig. DR5b).
102 Samples of the host rock ~50 cm away from the contact (HW10-23, 24) exhibit an

intermediate temperature component (Component A) that is similar to the dyke and a high-temperature component (Component B) similar to unbaked host rocks of the Nandaling Formation (Fig. DR5b). These observations indicate a positive baked contact test for a primary signal in the dyke. Furthermore, the ChRMs obtained from the sills (site HW03, HW07 and HW12) are all of normal polarity and are directionally distinct from the adjacent host rocks (HW02, HW11, HW06, HW08, HW09, HW13) that all exhibit reversed polarity (Table DR3). These observations suggest that the unbaked host rocks and the sills likely carry a primary magnetization. The ChRMs also pass fold tests (McElhinny, 1964; Watson and Enkin, 2003; McFadden, 1990) indicative of a pre-folding origin for the magnetization (Fig. 2B and Table DR3). A widely-distributed unconformity developed between the Jiulongshan and Xiahuayuan formations (~161 Ma) in North Hebei and under the Haifanggou Formation (~168 Ma) in West Liaoning, North China which was assigned as the first phase of the "Yanshan Movement" (Huang, 2019). The prefolding magnetization was therefore acquired prior to the Late Jurassic. Together with a "C" class positive reversal test (McFadden and McElhinny, 1990) (Table DR3), we interpret the ChRMs as primary.

Twenty-two sites were collected from the Tiaojishan Formation (HP01-HP22) over a large area near Pingquan in northern Hebei Province (Figs. DR1b) and 6 sites from the Lanqi Formation (LK01-06) near Jianchang in western Liaoning (Fig. DR1c). A total of 222 out of 282 specimens yield ChRMs that are statistically acceptable at site level. Eighteen out of 22 sites from Pingquan yield an interval-mean direction of D = 34.0 °, I = 65.0 °(α_{95} = 13.2 °) before and D = 38.4 °, I = 50.5 °(α_{95} = 8.1 °) after tilt correction. Five out of 6 sites from Jianchang yield interval-mean direction of D = 358.3 °, I = 57.8 °(α_{95} = 24.5 °) before and D = 33.0 °, I = 57.2 °(α_{95} = 14.9 °) after tilt

correction (Table DR4). The combined 23 sites yield a formation-mean direction of D = 24.5°, I = 64.2° (α_{95} = 11.3°) before and D = 37.4°, I = 52.0° (α_{95} = 6.8°) after tilt correction. The ChRMs pass both positive reversal and fold tests allowing us to interpret the remanence as primary (Table DR4).

Magnetizations resided in volcanic rocks are spot readings of the Earth's magnetic field. Paleosecular variations (PSV) therefore must be adequately sampled out before we get a reliable paleomagnetic pole. Statistical analysis on the virtual geomagnetic poles (Deenen et al., 2011; McFadden et al., 1991) of the Tiaojishan and Nandaling paleomagnetic poles suggests that the PSV was sufficiently averaged (Tables DR3 and DR4).

2.3 A review of paleomagnetic data from NCB and Amuria

Two previous paleomagnetic studies were reported from the early Jurassic sedimentary rocks near Datong, Shanxi Province (Uno and Huang, 2003) and Fuxian, Shaanxi Province (Ma et al., 1993). The ChRMs for the combined 15 sites yield a mean paleolatitude of 32 ± 5.5 °N (Uno and Huang, 2003) (at reference site of 40° N, 120° E). Inclination shallowing was not assessed in either study and these investigations lacked field tests and rock magnetic analysis. These data are therefore of limited use in ascertaining the paleoposition of NCB during the Early Jurassic. Four paleomagnetic studies were carried out on sedimentary sequences with a probable middle Jurassic age. Three of the four studies were based on limited sampling (no more than 6 sites) (Fang et al., 1988; Zheng et al., 1991; Yang et al., 1992) and are not used in our analysis. A more comprehensive study on sedimentary red beds yielded a paleolatitude estimate of 27.1 ± 6.4 °N for the NCB during the Middle Jurassic (Gilder and Courtillot, 1997) that is significantly lower than our estimate. That paper did not consider the possibility of inclination shallowing in the

153 red beds. Furthermore, the sampling sites occur stratigraphically above the coal-
154 bearing early to middle Jurassic strata suggesting that the rocks are more likely late
155 Middle Jurassic or Late Jurassic in age. In consideration of the above issues, we do
156 not consider these data further and argue that the NCB was located at 61.7 ± 9.1 °N
157 during the interval between 168-180 Ma.

158 Seven paleomagnetic poles based on volcanic rocks are available for NCB and
159 Amuria during the Late Jurassic (Table DR5). Of these seven studies, two poles
160 derived from sites located along the northern margin of Amuria near the Mongol-
161 Okhotsk suture zone (Kravchinsky et al., 2002; Cogné et al., 2005) are excluded due
162 to remagnetization. The Tiaojishan Formation was the focus of two previous studies
163 (Pei et a., 2011; Ren et al., 2016) that were combined to yield a paleolatitude for the
164 NCB at ~39.4 °± 5.6 °N (Ren et al., 2016). Paleomagnetic results from Manzhouli and
165 Hua'an, Inner Mongolia yielded a mean paleolatitude of ~27 ° N for Inner Mongolia
166 (Zhao et al., 1990). However, the age of the Inner Mongolian paleomagnetic pole
167 (Zhao et al., 1990) is poorly constrained. Our paleomagnetic data from the Tiaojishan
168 Formation yields a paleolatitude of 34.2 ± 7.9 °N. A mean paleomagnetic pole
169 calculated from 51 acceptable sites in the Tiaojishan Formation falls at 66.1 °N,
170 208.3 °E, A_{95}=5.1 °and a resultant paleolatitude at 36.6 ± 5.1 °N that is identical to our
171 study.

172 Our paleolatitude estimate for Late Jurassic is considerably lower than previous
173 inclination-corrected directions compiled from sedimentary rocks in East Asia (Van
174 der Voo et al., 2015). The discrepancy likely results from: 1) uncertainty in the use of
175 an arbitrarily assigned blanket flattening factor of f=0.6; 2) poorly constrained ages
176 for the sedimentary sequence that are mostly fossil-poor red beds and 3) use of a 20
177 Ma running mean window that averages critical variations in the apparent polar

wander paths. Ren et al. (2018) recently reported a Late Jurassic paleomagnetic pole from the Sharilyn Formation, southern Mongolia. The paleomagnetic pole is derived from a suite of red beds that is dated by $^{40}Ar/^{39}Ar$ method on a layer of tuff interbeds. Inclination shallowing was evaluated using the E-I method (Tauxe, 2005) and the calculated paleopole agrees well with our Tiaojishan paleomagnetic pole with a resultant paleolatitude of 32.9 ± 3.7 °N.

3. Environmental change in East Asia

The Jurassic and early Cretaceous sedimentary records in East Asia are illustrated in Fig. 1B. In North China, Lower and Middle Jurassic continental strata are characterized by dark, coal- and siderite-bearing strata rich in plant fossils indicative of a humid-temperate climate. An arid sequence featuring red beds, evaporite-bearing (gypsum and anhydrite) units and thick aeolian-sandstones overlies the humid-temperate facies creating a sharp contact between the dark and red units (Fig. 1B1-4) (e.g., Huang, 2019; Xu et al., 2013; 2019). The facies change occurred around ~155 Ma in the Junggar Basin along the boundary between the Qigu and Toutunhe formations (Huang, 2019). In the Chengde Basin (Yanliao area), the wet-dry transition predates major eruptions recorded in the Tiaojishan/Lanqi formations (~153-161 Ma) (Huang, 2019) that are intercalated with red beds and gypsum (Figs. 1B4 and DR2). The transition postdates the extinction of the underlying Yanliao biota that forms an important lagerstatte between ~160 and 168 Ma (Ji et al., 2006; Dong et al., 2014; Chu et al., 2016; Huang, 2019). In the Ningwu Basin (Shanxi), a zircon U-Pb age of 160.6 ± 0.55 Ma is reported from a layer of tuffaceous micrites directly below the boundary between the dark-colored Yungang and the purple-red Tianchihe formations (Li et al., 2014) (Fig. 1B3). In South China, the lower Jurassic Lishan Formation contains coal seams and siderite suggestive of warm and humid climate

whereas the upper Zhangping Formation (Bathonian and Oxfordian, ~168-163 Ma) is dominated by red beds and fossils of drought-resistant plants indicating gradual aridification (Deng et al., 2017) (Fig. 1B5). In the Qiangtang Basin at the southern margin of Jurassic Asia, a suite of marine-terrigenous carbonate and clastic rocks developed during the Middle to Late Jurassic. The Quemocuo Formation (Bajocian-Bathonian) is coal bearing whereas the upper part of the Xiali Formation (Callovian-Oxfordian) contains abundant gypsum suggestive of rapid aridification (Fang et al., 2016) (Fig. 1B6). This aridification can be traced northward to southern Mongolia (Traynor and Sladen, 1995) and westward to Iran (Mattei et al., 2014) and Central Asia (e.g., Brunet et al., 2017). The dramatic facies change is therefore recognizable over an area of ~10,000,000 square kilometers throughout East Asia between ~165-155 Ma. We call this transition the "Great Jurassic East Asian Aridification".

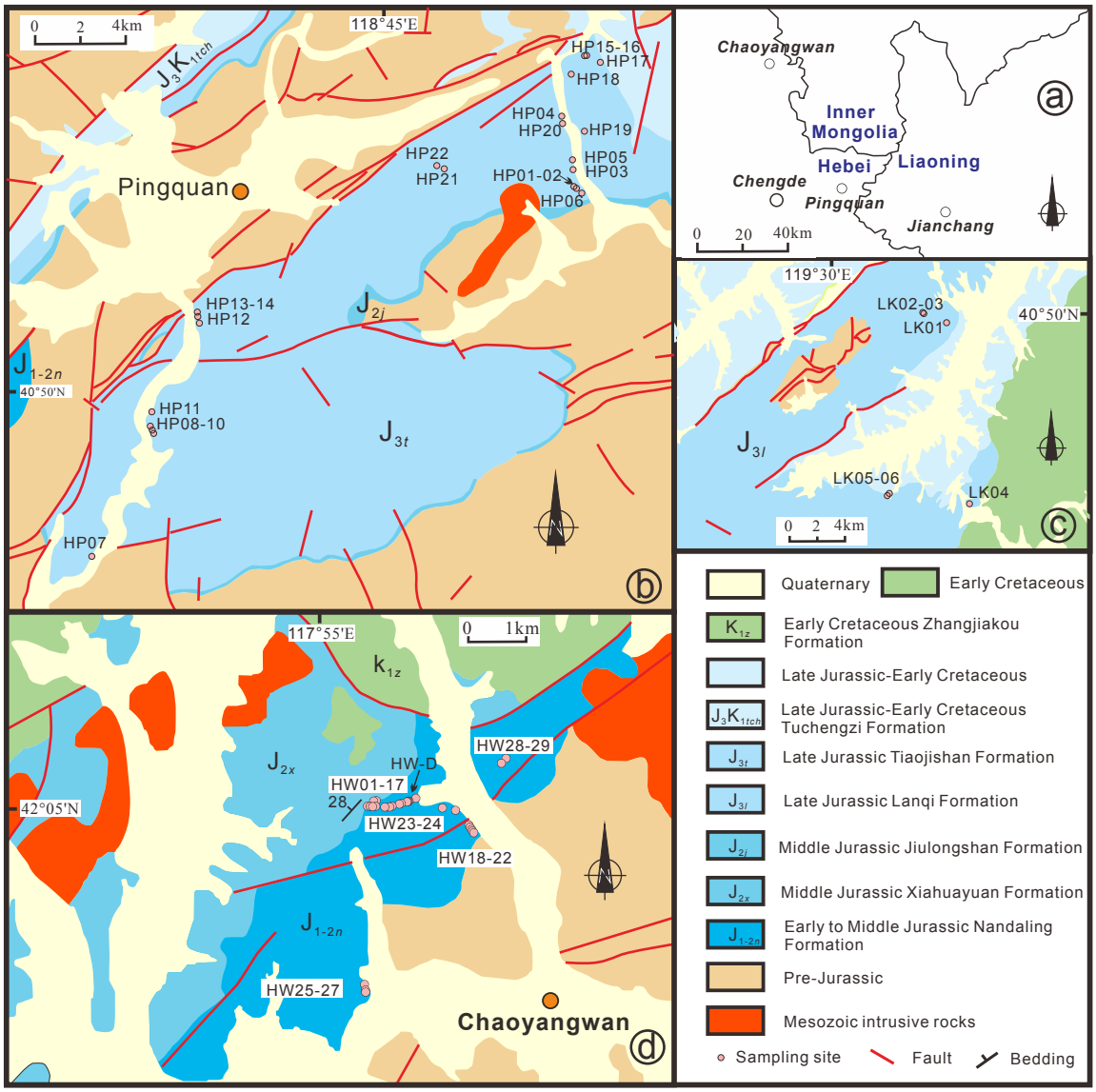

Figure DR1

Simplified administrative (a) and geological maps (b-d) illustrating the Mesozoic stratigraphy and paleomagnetic sampling locations in the (b) Pingquan, (c) Jiangchang and (d) Chaoyangwan areas, North China. HW-D was collected from a layer of tuffaceous sandstones at 42 °05.141′N, 117 °56.242′E.

Figure DR2

Field photos showing the lithology and bedding attitudes of the sampled outcrops of the Tiaojishan/Lanqi Formation. The bedding attitudes are measured in-situ or from the intercalated sedimentary layers near the sampled outcrop. Photos taken facing north (a) ; south (b); west (c); northeast (d); northeast (e); east (f); north (g); southwest (h); south (i); northeast (j); southeast (k); northwest (l).

Figure DR3

Field photos showing lithology and bedding attitudes of sampled outcrops within the Nandaling Formation. (a) Sites HW01-HW17 were sampled from a small valley. (b) The Xiahuayuan Formation conformably or paraconformably overlies the Nandaling Formation. (c, d) The Nandaling Formation was intruded by diabase dykes and (e) diorite sills. Photos taken facing (f) west and (g) southwest.

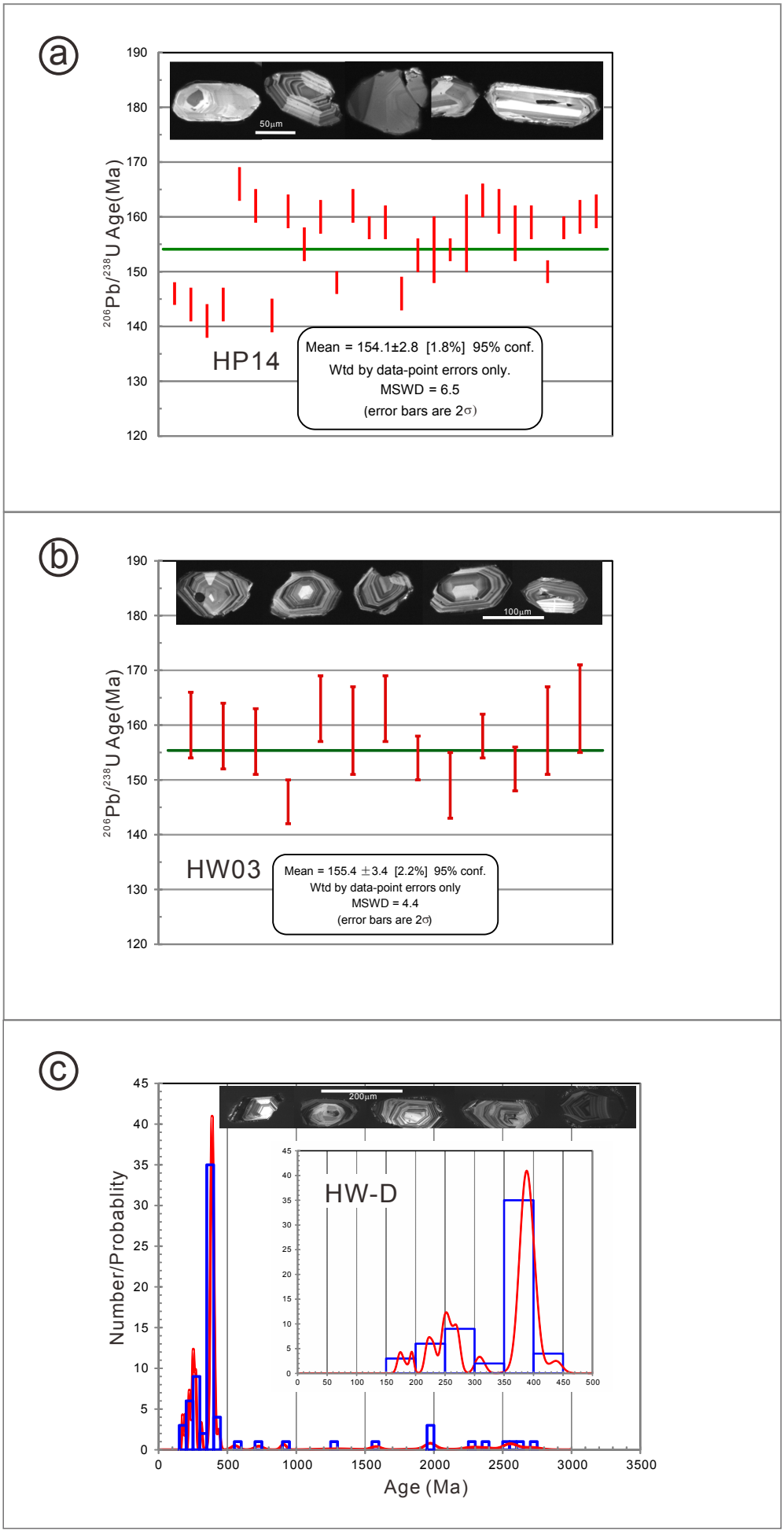
ⓐ
190
180
170
160
150
140
130
120
$^{206}Pb/^{238}U$ Age(Ma)
50μm
HP14
Mean = 154.1±2.8 [1.8%] 95% conf.
Wtd by data-point errors only.
MSWD = 6.5
(error bars are 2σ)
ⓑ
190
180
170
160
150
140
130
120
$^{206}Pb/^{238}U$ Age(Ma)
100μm
HW03
Mean = 155.4 ±3.4 [2.2%] 95% conf.
Wtd by data-point errors only
MSWD = 4.4
(error bars are 2σ)
ⓒ
45
40
35
30
25
20
15
10
5
0
Number/Probablity
200μm
HW-D
0
50
100
150
200
250
300
350
400
450
500
0
500
1000
1500
2000
2500
3000
3500
Age (Ma)

Figure DR4

LA-ICP-MS zircon U-Pb dating results of (a) the Tiaojishan Formation (HP14), (b) the sills (HW03) intruding the Nandaling Formation and (c) the Nandaling (HW-D) Formation. See Table DR1 for details.

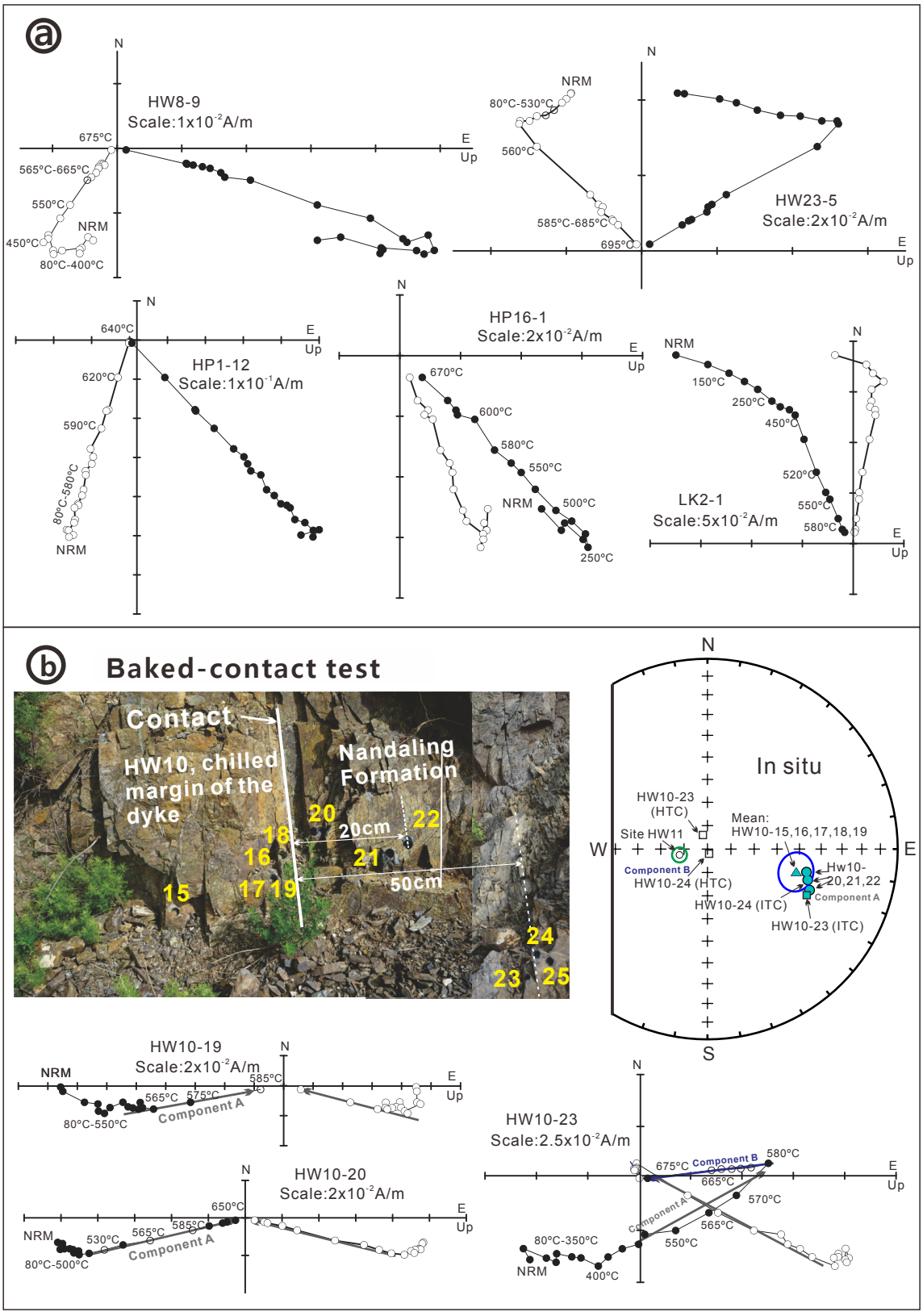

Figure DR5

(a) Orthogonal (Zijderveld) vector plots of representative specimens from the Nandaling and Tiaojishan formations. Directions are plotted in geographic

coordinates; open and solid circles represent vectors and endpoints projected onto vertical and horizontal planes, respectively. (b) A baked contact test performed at site HW10 showing gradual change of ChRMs of the dyke and the baked, half-baked and unbaked host rocks of the Nandaling Formation suggestive of inverse baked contact test and a primary magnetic signal in the dyke. ITC and HTC represent intermediate and high temperature components defined from the demagnetization trajectory of HW10-23 and HW10-24. Lines with grey (Component A) and blue (Component B) arrows represent the interpreted vectors defined from the demagnetization trajectories. See more explanations in the Data Repository text.

295
296
297
298

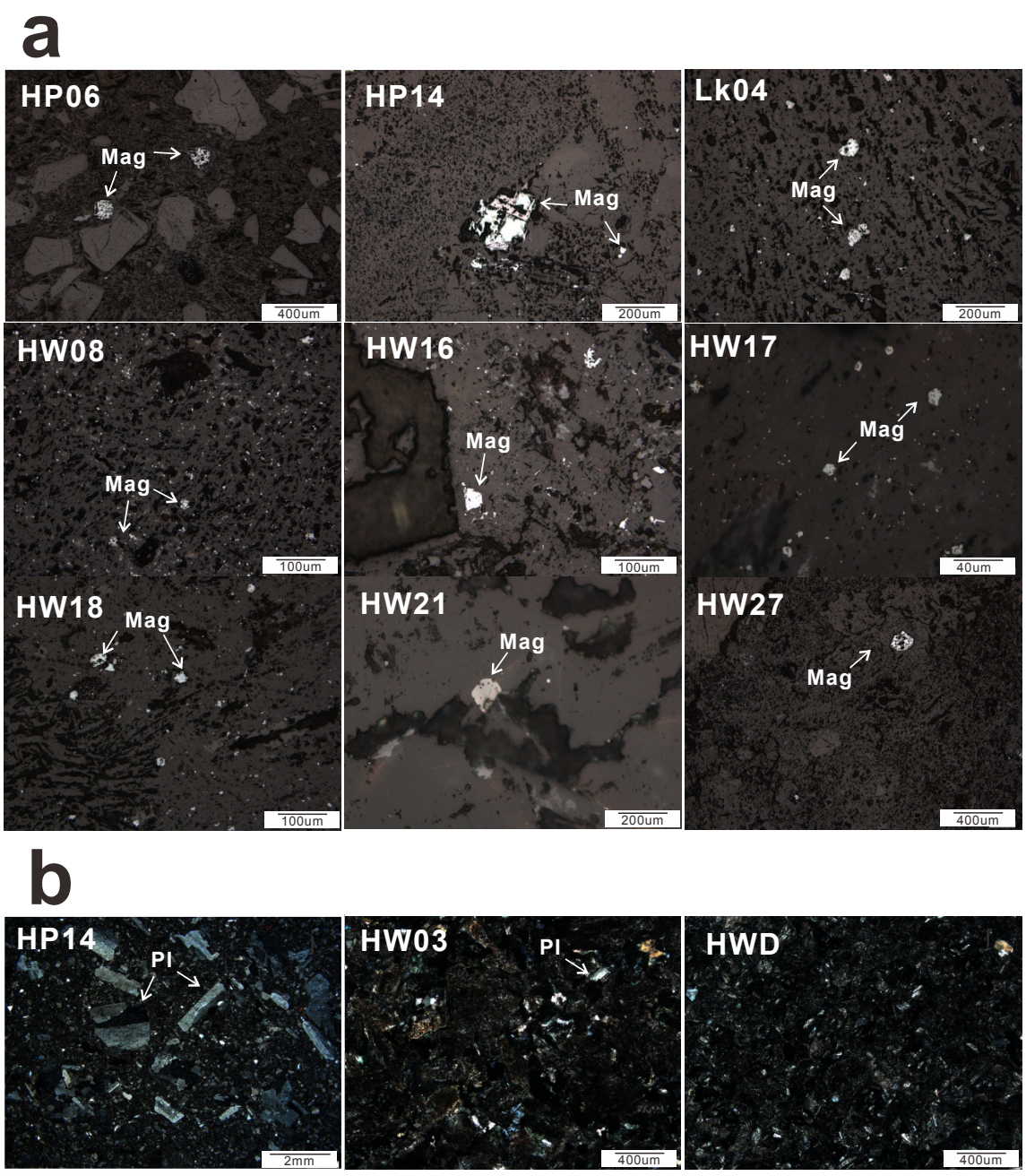

299 **Figure DR6**

300 (a) Photomicrographs for the volcanic rocks from the Tiaojishan/Lanqi and
301 Nandaling Formations. Magnetites are idiomorphic in shape, indicative of magmatic
302 origin. In addition, no obvious alteration minerals (e.g. chlorite, etc) are observed. (b)
303 Photomicrographs of volcanic rock samples HP14 (Tiaojishan Formation), HW03 (sill

intruding the Nandaling Formation) and HWD (Nandaling Formation). These three samples were used to select the zircons for LA-ICP-MS U-Pb dating. Abbreviations: Mag, magnetite; and Pl, plagioclase.

Table DR1: LA-ICP-MS zircon U-Pb dating results of volcanic rocks from the Tiaojishan and Nandaling formations and the sills intruding the Nandaling Formation, North China.

Sample No.	CORRECTED RATIOS						CORRECTED AGES (Ma)						Th	U	Th/U
	$^{207}Pb/^{206}Pb$		$^{207}Pb/^{235}U$		$^{206}Pb/^{238}U$		$^{207}Pb/^{206}Pb$		$^{207}Pb/^{235}U$		$^{206}Pb/^{238}U$				
	Ratio	1σ	Ratio	1σ	Ratio	1σ	Age (Ma)	1σ	Age (Ma)	1σ	Age (Ma)	1σ			
HP14-01	0.05020	0.00218	0.15854	0.00679	0.02291	0.00038	204	68	149	6	146	2	206.47	81.32	2.54
HP14-02	0.05857	0.00377	0.18288	0.01140	0.02265	0.00051	551	97	171	10	144	3	403.80	121.01	3.34
HP14-03	0.04917	0.00533	0.15038	0.01622	0.02219	0.00042	156	207	142	14	141	3	157.29	69.57	2.26
HP14-04	0.06385	0.00440	0.19844	0.01319	0.02255	0.00054	737	100	184	11	144	3	86.45	48.49	1.78
HP14-06	0.04937	0.00253	0.17753	0.00893	0.02609	0.00048	165	83	166	8	166	3	102.06	45.71	2.23
HP14-07	0.04971	0.00338	0.17421	0.01161	0.02543	0.00053	181	113	163	10	162	3	96.20	51.45	1.87
HP14-08	0.05052	0.00315	0.15545	0.00943	0.02232	0.00047	219	101	147	8	142	3	310.68	106.33	2.92
HP14-09	0.04940	0.00250	0.17264	0.00859	0.02536	0.00046	167	82	162	7	161	3	71.46	35.73	2.00
HP14-10	0.05169	0.00204	0.17286	0.00676	0.02426	0.00040	272	59	162	6	155	3	238.77	80.16	2.98
HP14-11	0.04809	0.00204	0.16650	0.00696	0.02512	0.00042	104	65	156	6	160	3	144.45	65.28	2.21
HP14-12	0.04942	0.00213	0.15830	0.00675	0.02324	0.00039	168	68	149	6	148	2	197.39	76.65	2.58
HP14-13	0.04991	0.00255	0.17451	0.00875	0.02537	0.00047	191	82	163	8	162	3	164.91	106.79	1.54
HP14-14	0.05036	0.00158	0.17188	0.00541	0.02476	0.00037	212	45	161	5	158	2	308.47	146.67	2.10
HP14-15	0.04966	0.00227	0.17057	0.00774	0.02492	0.00041	179	75	160	7	159	3	135.54	62.14	2.18
HP14-16	0.04896	0.00343	0.15499	0.01058	0.02296	0.00052	146	112	146	9	146	3	210.40	75.08	2.80
HP14-17	0.04920	0.00253	0.16321	0.00823	0.02406	0.00046	157	81	154	7	153	3	429.10	123.14	3.48
HP14-18	0.04846	0.00666	0.16110	0.02141	0.02412	0.00094	122	221	152	19	154	6	114.42	39.77	2.88
HP14-20	0.06078	0.00147	0.20281	0.00502	0.02420	0.00036	631	29	188	4	154	2	386.36	141.55	2.73
HP14-21	0.04905	0.01192	0.16623	0.03982	0.02458	0.00109	150	360	156	35	157	7	154.77	50.22	3.08
~~HP14-22~~	~~0.00330~~	~~0.00394~~	~~0.01004~~	~~0.01197~~	~~0.02206~~	~~0.00040~~	~~1773~~	~~281~~	~~10~~	~~12~~	~~141~~	~~3~~	~~299.71~~	~~95.75~~	~~3.13~~
HP14-23	0.04949	0.00202	0.17450	0.00710	0.02558	0.00042	171	64	163	6	163	3	128.62	56.42	2.28
HP14-24	0.05412	0.00438	0.18889	0.01481	0.02532	0.00069	376	128	176	13	161	4	112.01	68.48	1.64
HP14-25	0.05122	0.00589	0.17393	0.01940	0.02463	0.00083	251	189	163	17	157	5	127.30	54.67	2.33
HP14-26	0.04894	0.00341	0.16835	0.01151	0.02495	0.00052	145	115	158	10	159	3	57.26	31.74	1.80
HP14-27	0.07060	0.00221	0.22855	0.00711	0.02348	0.00038	946	38	209	6	150	2	144.55	71.75	2.01
HP14-28	0.04910	0.00185	0.16776	0.00623	0.02478	0.00039	153	57	157	5	158	2	241.78	121.84	1.98

HP14-29	0.05091	0.00187	0.17621	0.00641	0.02510	0.00040	237	55	165	6	160	3	208.46	81.04	2.57
HP14-30	0.05849	0.00295	0.20379	0.01003	0.02527	0.00050	548	73	188	8	161	3	88.70	47.81	1.86
HW03-2	0.04940	0.00301	0.17126	0.01017	0.02515	0.00053	167	97	161	9	160	3	118.52	51.07	2.32
HW03-3	0.04954	0.00297	0.16915	0.00991	0.02478	0.00052	173	96	159	9	158	3	237.87	99.04	2.40
HW03-4	0.08774	0.00252	0.29853	0.00848	0.02468	0.00040	1377	31	265	7	157	3	191.81	75.88	2.53
HW03-5	0.04874	0.00204	0.15361	0.00632	0.02286	0.00038	135	65	145	6	146	2	41.52	52.02	0.80
HW03-6	0.04939	0.00265	0.17402	0.00914	0.02556	0.00050	166	85	163	8	163	3	100.77	54.18	1.86
HW03-7	0.04897	0.00412	0.16864	0.01379	0.02499	0.00066	146	134	158	12	159	4	74.28	83.85	0.89
HW03-8	0.04203	0.00221	0.14838	0.00775	0.02561	0.00042	-175	88	140	7	163	3	247.86	79.27	3.13
HW03-9	0.05435	0.00194	0.18166	0.00647	0.02425	0.00038	386	52	169	6	154	2	207.45	61.55	3.37
~~HW03-10~~	~~0.05369~~	~~0.00086~~	~~0.43703~~	~~0.00773~~	~~0.05904~~	~~0.00080~~	~~358~~	~~19~~	~~368~~	~~5~~	~~370~~	~~5~~	244.46	297.24	0.82
HW03-11	0.05102	0.00284	0.16475	0.00893	0.02342	0.00045	242	89	155	8	149	3	43.95	44.75	0.98
HW03-12	0.05012	0.00138	0.17163	0.00481	0.02484	0.00037	201	38	161	4	158	2	218.30	159.71	1.37
HW03-13	0.04979	0.00183	0.16408	0.00603	0.02390	0.00038	185	56	154	5	152	2	60.76	74.67	0.81
HW03-14	0.05052	0.00375	0.17444	0.01263	0.02504	0.00061	219	120	163	11	159	4	134.26	59.91	2.24
HW03-15	0.04918	0.00427	0.17382	0.01470	0.02564	0.00064	156	143	163	13	163	4	69.62	30.37	2.29
HW-D-02	0.05501	0.00060	0.46962	0.01085	0.06192	0.00134	413	19	391	8	387	8	405.58	676.14	0.60
HW-D-03	0.05424	0.00062	0.47133	0.01243	0.06300	0.00142	389	28	392	9	394	9	156.25	377.42	0.41
HW-D-04	0.04937	0.00059	0.20770	0.00430	0.03050	0.00053	165	14	192	4	194	3	113.74	880.34	0.13
HW-D-05	0.04978	0.00122	0.18676	0.00596	0.02721	0.00070	183	56	174	5	173	4	96.82	191.94	0.50
HW-D-07	0.05470	0.00094	0.46066	0.01195	0.06107	0.00123	398	46	385	8	382	8	85.26	153.95	0.55
HW-D-08	0.15917	0.00234	7.83491	0.74643	0.35594	0.02995	2447	30	2212	86	1963	142	65.63	142.62	0.46
HW-D-09	0.05475	0.00103	0.46063	0.01818	0.06097	0.00165	467	37	385	13	382	10	138.68	437.13	0.32
HW-D-10	0.05185	0.00100	0.28956	0.00880	0.04049	0.00092	280	-116	258	7	256	6	185.69	196.77	0.94
HW-D-11	0.05407	0.00072	0.45184	0.01144	0.06061	0.00139	372	51	379	8	379	9	102.39	389.75	0.26
HW-D-12	0.15123	0.00161	7.46532	0.19283	0.35789	0.00758	2361	-5	2169	24	1972	36	69.82	210.44	0.33
HW-D-13	0.10827	0.00308	3.35137	0.44855	0.22260	0.02423	1772	49	1493	105	1296	128	65.35	197.93	0.33
HW-D-14	0.05500	0.00207	0.45992	0.01861	0.06065	0.00125	413	83	384	13	380	8	32.10	33.53	0.96
HW-D-15	0.05463	0.00126	0.32076	0.01087	0.04257	0.00092	398	56	282	8	269	6	190.25	219.80	0.87

HW-D-16	0.05394	0.00085	0.47085	0.01187	0.06329	0.00126	369	37	392	8	396	8	112.40	150.55	0.75
HW-D-17	0.05383	0.00096	0.46732	0.01378	0.06297	0.00170	365	14	389	10	394	10	135.22	175.02	0.77
HW-D-19	0.05442	0.00064	0.45962	0.01216	0.06124	0.00147	387	28	384	9	383	9	688.63	946.58	0.73
HW-D-20	0.06213	0.00292	0.53071	0.03539	0.06181	0.00168	680	102	432	24	387	10	26.24	111.75	0.23
HW-D-21	0.05429	0.00081	0.46101	0.01258	0.06157	0.00141	383	37	385	9	385	9	215.32	423.03	0.51
HW-D-22	0.05196	0.00092	0.30146	0.00919	0.04206	0.00093	283	60	268	7	266	6	299.77	365.02	0.82
HW-D-23	0.05649	0.00162	0.55013	0.02356	0.07057	0.00145	472	65	445	16	440	9	185.80	209.81	0.89
HW-D-24	0.05137	0.00070	0.28354	0.00693	0.04002	0.00077	257	37	253	6	253	5	527.68	443.52	1.19
HW-D-25	0.05469	0.00104	0.49180	0.01199	0.06521	0.00104	398	46	406	8	407	6	83.43	114.32	0.73
HW-D-26	0.05151	0.00132	0.27618	0.00836	0.03888	0.00064	265	56	248	7	246	4	80.95	109.56	0.74
HW-D-27	0.05416	0.00106	0.46421	0.01227	0.06216	0.00124	376	46	387	9	389	8	126.38	127.77	0.99
HW-D-28	0.05404	0.00084	0.46529	0.01374	0.06243	0.00150	372	60	388	10	390	9	285.92	197.70	1.45
HW-D-29	0.05163	0.00084	0.28166	0.00674	0.03957	0.00070	333	37	252	5	250	4	1065.26	479.68	2.22
HW-D-30	0.16830	0.00185	11.29929	0.28438	0.48687	0.01080	2543	19	2548	25	2557	47	285.32	325.11	0.88
HW-D-31	0.05163	0.00071	0.30568	0.00744	0.04294	0.00081	333	37	271	6	271	5	780.64	585.91	1.33
HW-D-32	0.06034	0.00079	0.53235	0.01149	0.06398	0.00107	617	28	433	8	400	7	3228.43	2187.89	1.48
HW-D-33	0.05422	0.00061	0.46630	0.00968	0.06237	0.00113	389	19	389	7	390	7	397.00	711.43	0.56
HW-D-35	0.05073	0.00128	0.24257	0.00762	0.03468	0.00074	228	56	221	6	220	5	74.53	140.69	0.53
HW-D-36	0.09799	0.00254	1.61999	0.10916	0.11955	0.00541	1587	49	978	42	728	31	64.00	118.85	0.54
HW-D-38	0.05718	0.00243	0.48643	0.04443	0.06137	0.00289	498	93	402	30	384	18	153.35	425.05	0.36
HW-D-39	0.05421	0.00086	0.44773	0.01097	0.05990	0.00127	389	37	376	8	375	8	205.30	262.28	0.78
HW-D-40	0.05233	0.00123	0.35875	0.01121	0.04972	0.00119	298	23	311	8	313	7	91.70	133.02	0.69
HW-D-41	0.16587	0.00168	10.18959	0.34021	0.44533	0.01315	2516	19	2452	32	2374	59	108.90	612.91	0.18
HW-D-42	0.05361	0.00069	0.45388	0.01282	0.06139	0.00161	354	28	380	9	384	10	236.90	512.11	0.46
HW-D-43	0.05417	0.00072	0.47601	0.01224	0.06371	0.00149	389	28	395	9	398	9	116.19	283.13	0.41
HW-D-45	0.05426	0.00088	0.46969	0.01523	0.06277	0.00201	383	37	391	11	392	12	105.41	195.32	0.54
HW-D-46	0.06824	0.00077	1.42324	0.03725	0.15121	0.00363	876	19	899	16	908	20	304.09	242.64	1.25
HW-D-47	0.05388	0.00064	0.45109	0.01088	0.06070	0.00142	365	28	378	8	380	9	303.34	472.79	0.64
HW-D-48	0.05699	0.00242	0.48532	0.03153	0.06161	0.00190	500	93	402	22	385	12	74.15	194.89	0.38
HW-D-49	0.05397	0.00076	0.46050	0.01450	0.06185	0.00179	369	28	385	10	387	11	104.83	330.43	0.32
HW-D-50	0.05451	0.00058	0.46472	0.01326	0.06180	0.00178	391	28	388	9	387	11	307.25	1152.22	0.27

HW-D-51	0.05348	0.00076	0.45679	0.01240	0.06194	0.00164	350	28	382	9	387	10	130.12	266.15	0.49
HW-D-52	0.05435	0.00125	0.28698	0.00913	0.03830	0.00102	387	46	256	7	242	6	1126.55	897.74	1.25
HW-D-53	0.05547	0.00139	0.37114	0.01263	0.04851	0.00111	432	56	320	9	305	7	1591.51	1005.83	1.58
HW-D-54	0.05556	0.00078	0.48125	0.01516	0.06278	0.00150	435	37	399	10	393	9	290.54	784.53	0.37
HW-D-55	0.05416	0.00123	0.30833	0.01095	0.04126	0.00087	389	46	273	9	261	5	338.79	417.98	0.81
HW-D-56	0.14958	0.00146	8.68922	0.28933	0.42104	0.01196	2343	19	2306	31	2265	55	552.04	425.13	1.30
HW-D-57	0.05189	0.00063	0.44536	0.01200	0.06224	0.00170	280	28	374	9	389	10	172.14	359.42	0.48
HW-D-59	0.04852	0.00053	0.27001	0.00619	0.04034	0.00086	124	28	243	5	255	5	2291.61	1557.07	1.47
HW-D-60	0.04820	0.00088	0.28714	0.00702	0.04319	0.00097	109	37	256	6	273	6	202.57	277.47	0.73
HW-D-61	0.15673	0.00362	7.76061	0.24610	0.35901	0.00880	2421	40	2204	29	1977	42	380.58	559.09	0.68
HW-D-62	0.05541	0.00206	0.48367	0.02142	0.06328	0.00161	428	106	401	15	396	10	88.50	170.81	0.52
HW-D-63	0.05027	0.00146	0.24417	0.00907	0.03521	0.00087	206	65	222	7	223	5	411.48	331.02	1.24
HW-D-64	0.05411	0.00128	0.47015	0.01583	0.06299	0.00161	376	56	391	11	394	10	530.08	600.59	0.88
HW-D-65	0.09737	0.00190	3.72784	0.11545	0.27753	0.00711	1576	37	1577	25	1579	36	151.80	1548.57	0.10
HW-D-66	0.16338	0.00347	11.20404	0.37676	0.49718	0.01451	2491	36	2540	33	2602	63	66.01	64.93	1.02
HW-D-67	0.05478	0.00189	0.48794	0.02167	0.06458	0.00200	467	74	404	15	403	12	322.96	232.59	1.39
HW-D-68	0.07473	0.00505	0.29346	0.02468	0.02841	0.00108	1061	132	261	19	181	7	729.37	222.20	3.28
HW-D-69	0.05394	0.00161	0.46258	0.02019	0.06219	0.00236	369	88	386	14	389	14	138.70	338.66	0.41
HW-D-70	0.05365	0.00163	0.44981	0.02191	0.06077	0.00245	367	65	377	15	380	15	395.82	537.78	0.74
HW-D-71	0.05489	0.00157	0.47584	0.02045	0.06286	0.00232	409	65	395	14	393	14	249.47	405.80	0.61
HW-D-72	0.05066	0.00150	0.24882	0.01036	0.03561	0.00118	233	65	226	8	226	7	761.11	476.06	1.60
HW-D-73	0.05476	0.00151	0.48272	0.01905	0.06393	0.00218	467	56	400	13	399	13	272.85	395.39	0.69
HW-D-74	0.05375	0.00121	0.46495	0.01622	0.06271	0.00184	361	56	388	11	392	11	910.93	811.70	1.12
HW-D-75	0.07387	0.00210	0.91801	0.05889	0.08997	0.00458	1039	56	661	31	555	27	38.04	140.00	0.27
HW-D-76	0.05388	0.00145	0.46060	0.01584	0.06198	0.00143	365	88	385	11	388	9	222.81	444.09	0.50
HW-D-77	0.15995	0.00329	10.65190	0.29968	0.48280	0.01041	2455	35	2493	27	2539	46	74.32	69.30	1.07
HW-D-78	0.05610	0.00162	0.53833	0.02287	0.06957	0.00226	457	88	437	15	434	14	124.60	237.46	0.52
HW-D-79	0.05180	0.00196	0.26024	0.01104	0.03642	0.00072	276	93	235	9	231	5	412.82	323.98	1.27
HW-D-80	0.16602	0.00369	12.04543	0.40259	0.52593	0.01298	2518	39	2608	33	2724	55	943.94	967.40	0.98

Table DR2: Isotopic and magnetostratigraphic ages for Jurassic rocks in East Asia.

NO.	Unit	Method	Age (Ma)	Reference
1	Qigu Fm	U-Pb (detrital Zircon)	<151	(Fang et al., 2015)
2	Qigu Fm	U-Pb	164.6±1.4	(Wang et al., 2012)
3	Badaowan	Ar-Ar	192.7±1.3	(Xu et al., 2008)
4	Yungang Fm	U-Pb	160.6±0.6	(Li et al., 2014)
5	Yongdingzhuang Fm	U-Pb	179.2±0.8	(Li et al., 2014)
6	Zhangjiakou Fm	Ar-Ar	139.4±0.19	(Swisher et al., 2002)
7	Tuchengzi Fm	U-Pb	153.7±1.1	(Xu et al., 2012)
8	Tiaojishan Fm (Top)	U-Pb	152±2.6	(Liu and Liu, 2005)
9	Tiaojishan Fm(Bottom)	U-Pb	160.254±0.045, 160.383±0.062, 160.889±0.069	(Chu et al., 2016)
10	Xiahuanyuan Fm	U-Pb (detrital Zircon)	175	(Lin et al., 2018)
11	Xiahuanyuan Fm	U-Pb (detrital Zircon)	194	(Lin et al., 2018)
12	Nandaling Fm	U-Pb/Ar-Ar	168-180	(Gao et al., 2018a, b; Huang, 2019) and references therein
13	Xueshan Fm	Magnetostratigraphy	<158	(Fang et al., 2016)
14	Xiali Fm	Magnetostratigraphy	160	(Fang et al., 2016)
15	Buqu Fm	Magnetostratigraphy	163	(Fang et al., 2016)
16	Quemocuo Fm	Magnetostratigraphy	166	(Fang et al., 2016)
17	Quemocuo Fm	Magnetostratigraphy	>171	(Fang et al., 2016)

The numbers are labeled in Figure 1B. For more isotopic ages from the Tiaojishan/Lanqi and Nandaling formations see Gao et al. (2018a, b), Huang et al. (2019) and references therein.

317 **Table DR3: Summary of the site-mean directions of ChRMs and VGPs from the Nandaling Formation, North China**

Site ID	Depth(m)	Lithology/color	GPS		Strike/dip	n/n0	N/R	Dg(°)	Ig(°)	Ds(°)	Is(°)	κ	α_{95}(°)	Plat. (°)	Plong. (°)
			Latitude	Longitude											
HW01	3	Basalt/Greyish green	42°05.106′N	117°55.803′E	200/28	7/8	0/7	260.5	-78.3	128.1	-71.3	105.6	5.9	-54.3	248.9
HW02	38	Tuff/Red	42°05.095′N	117°55.851′E	218/27	10/10	0/10	237.9	-87.1	134.3	-63.9	162.5	3.8	-57.3	230.0
[a]HW03	46	Diorite Sill	42°05.096′N	117°55.862′E	226/29	8/9	9/0	53.2	69.5	355.9	57.2	135.2	4.8	87.4	335.4
[b]HW10	48	Diabase Dyke	42°05.116′N	117°55.880′E	229/28	11/17	11/0	94.0	59.2	36.0	68.2	43.8	7.0	63.5	174.8
HW11	49	Basalt/Greyish red	42°05.117′N	117°55.884′E	229/28	8/8	0/8	258.2	-77.8	165.7	-65.7	300.4	3.2	-78.4	242.9
HW04	82	Andesite/Greyish black	42°05.087′N	117°55.903′E	203/33	7/7	0/7	280.1	-65.8	142.6	-79.3	316.0	3.4	-56.7	275.0
HW05	135	Andesite/Greyish red	42°05.088′N	117°55.979′E	199/26	9/11	0/9	260.1	-61.8	195.3	-76.7	548.2	2.2	-65.8	313.9
HW06	167	Tuff/Red	42°05.075′N	117°56.023′E	216/27	10/10	0/10	269.0	-71.7	168.3	-73.7	116.2	4.5	-71.0	279.6
[a]HW07	179	Diorite Sill	42°05.065′N	117°56.033′E	231/28	9/9	9/0	40.5	69.8	355.4	53.0	427.4	2.5	80.7	332.4
HW08	196	Tuff/Red	42°05.058′N	117°56.058′E	231/28	10/11	0/10	248.9	-76.2	171.1	-63.1	162.5	3.8	-83.1	232.1
HW09	267	Tuff/Greyish green	42°05.087′N	117°56.152′E	231/28	8/9	3/5	90.4	70.7	5.8	68.7	52.7	7.7	79.3	137.5
[a]HW12	272	Diorite Sill	42°05.101′N	117°56.171′E	231/28	9/9	9/0	39.4	75.4	347.3	56.2	215.3	3.5	78.8	3.5
HW13	304	Andesite/Greyish red	42°05.109′N	117°56.218′E	239/36	7/10	0/7	282.7	-31.8	254.1	-50.5	67.5	7.4	-31.4	12.5
HW14	306	Andesite/Greyish red	42°05.108′N	117°56.224′E	239/36	7/7	0/7	308.9	-56.9	216.5	-78.3	207.4	4.2	-57.9	323.3
HW15	308	Andesite/Greyish black	42°05.111′N	117°56.230′E	239/36	8/8	0/8	306.1	-59.6	205.6	-76.4	134.1	4.8	-63.5	322.9
HW16	310	Andesite/Greyish black	42°05.106′N	117°56.235′E	239/36	10/10	0/10	310.5	-56.0	220.6	-79.3	57.9	6.4	-55.7	322.0
HW17	340	Andesite/Greyish red	42°05.108′N	117°56.292′E	212/29	6/9	6/0	101.2	62.7	13.0	80.1	100.9	6.7	60.6	126.6
HW23	Unknown	Andesite/Greyish red	42°04.983′N	117°56.392′E	239/36	11/11	0/11	307.9	-53.8	231.3	-77.6	181.2	3.4	-53.2	329.5
HW24	Unknown	Andesite/Greyish black	42°04.960′N	117°56.516′E	192/62	10/10	0/10	252.2	-7.3	222.6	-55.0	32.5	8.6	-56.5	24.8
HW18	Unknown	Andesite/Greyish red	42°04.788′N	117°56.676′E	208/39	8/8	0/8	291.4	-62.9	132.2	-77.5	166.8	4.3	-54.6	266.8
HW19	Unknown	Andesite/Greyish red	42°04.759′N	117°56.679′E	214/40	7/8	0/7	284.7	-60.9	161.5	-74.7	189.1	4.4	-67.8	274.2

HW20	Unknown	Andesite/Greyish green	42°04.727′N	117°56.719′E	222/40	10/10	10/0	97.0	40.0	50.7	63.6	45.3	7.3	53.8	185.3
HW21	Unknown	Andesite/Greyish green	42°04.722′N	117°56.726′E	222/40	6/8	6/0	110.9	29.9	87.6	64.8	44.4	11.6	30.6	170.7
HW22	Unknown	Andesite/Greyish green	42°04.699′N	117°56.737′E	219/34	10/10	10/0	77.2	53.8	21.3	60.8	45.2	7.3	74.2	201.7
HW25	Unknown	Conglomerate tuff/Greyish red	42°03.410′N	117°55.326′E	226/39	7/9	--	--	--	--	--	--	--	--	--
HW26	Unknown	Tuff/Greyish red	42°03.424′N	117°55.375′E	54/18	8/9	8/0	12.5	78.7	104.7	76.6	89.1	5.9	31.6	147.2
HW27	Unknown	Tuff/Greyish red	42°03.419′N	117°55.355′E	226/39	6/9	6/0	113.6	49.3	43.8	75.6	281.4	4.0	57.2	153.7
HW28	Unknown	Andesite/Greyish red	42°05.305′N	117°57.217′E	215/36	7/9	0/7	275.0	-48.9	218.0	-70.8	135.7	5.2	-62.2	346.8
HW29	Unknown	Andesite/Greyish red	42°05.285′N	117°57.194′E	215/36	7/8	0/7	282.8	-50.0	222.4	-75.8	316.0	3.4	-57.7	332.7
Mean for volcanic rocks (without a and b)						24/25	7/17	**100.1**	**59.9**			**15.2**	**7.8**	**65.9**	**140.3**
										21.9	**75.3**	**29.3**	**5.6**	**K=11.6**	**A_{95}=9.1**
Mean a (intruded sills, 155Ma)						3/3	3/0	44.9	71.7			384.1	6.3		
										352.9	55.5	538.4	5.3		

1. Fold tests:
(1) Watson and Enkin's Test (2003): the optimal concentration is achieved at 99.0 ±6.4% unfolding level;
(2) McElhiny's Test (1964): N=24, *ks/kg*=1.93 > F [46, 46] = 1.64 indicative of a positive fold test at 95% confidence level;
(3) McFadden's Test (1990): N=24, in-situ ξ_2=13.29, tilt-corrected ξ_2=3.71, statistical threshold ξ =8.0 at 99% confidence level, indicative of a positive fold test.
2. Reversal test (McFadden and McElhinny, 1990): the angular difference of 9.5 °between the normal and reversed polarities is less than the critical angle of 12.0 °indicative of a positive reversal test of C class.
3. PSV analysis (Deenen et al., 2011): the Deenen's envelope for N=24 is 4.8 to 11.1 and the A_{95} for the Nandaling paleopole is 9.1 suggesting that the PSV has been sampled out.
4. PSV analysis (McFadden et al., 1991): the VGP Scatter (S) for the Nandaling pole is 23.7 and the acceptable S suggested by Model G is from 17.8 to 23.7, suggesting that the PSV has been sampled out.
Depth, vertical distance from sampling position to the upper boundary of the Nandaling Formation.
Abbreviations are: Site ID, Site identification; Strike/dip, strike azimuth and dip of bed; n/n_0, number of samples or sites used to calculate site-mean or interval-mean ChRMs/number of samples or sites demagnetized; N/R, number of samples or sites showing normal/reversed polarity; Dg and Ig (Ds and Is), κ_s, α_{95s}, declination and inclination of direction in-situ (after tilt adjustment), precision parameter, 95% confidence limit of

Fisher statistics. Plat. and Plong. are latitude and longitude of VGP in stratigraphic coordinates. A_{95}, 95% confidence limit of VGPs using Fisher statistics

Table DR4: Summary of site-mean directions of ChRMs and VGPs from the Tiaojishan and Lanqi formations (~153-161Ma), North China

Site ID	Lithology/Color	GPS		Strike/dip	n/n_0	N/R	Dg(°)	Ig(°)	Ds(°)	Is(°)	κ	α_{95}(°)	Plat. (°)	Plong. (°)
		Latitude	Longitude											
Pingquan, northern Hebei, Tiaojishan Formation														
HP01	Andesite/Greyish red	40°54.790′N	118°51.766′E	297/19	9/11	0/9	207.1	-47.4	207.0	-28.4	116.0	4.8	-55.2	68.8
HP02	Andesite/Greyish red	40°54.787′N	118°51.601′E	288/20	11/11	0/11	204.4	-43.5	203.0	-23.5	521.6	2.0	-55.0	77.2
[a]HP03	Basalt/Greyish black	Unavailable		296/27	4/11	0/4	~~160.5~~	~~-35.1~~	~~168.9~~	~~-14.5~~	~~33.3~~	~~21.7~~	~~-55.0~~	~~138.4~~
HP04	Basalt/Greyish red	40°56.582′N	118°51.079′E	285/29	9/9	9/0	40.0	77.8	23.0	49.6	259.7	3.2	68.7	231.0
HP05	Basalt/Greyish black	40°55.671′N	118°51.455′E	290/27	7/7	0/7	258.7	-60.8	233.8	-41.5	146.7	5.0	-42.3	32.6
HP06	Andesite/Greyish red	40°54.733′N	118°51.688′E	297/19	7/8	0/7	214.5	-56.7	212.0	-37.8	335.4	3.3	-56.6	55.2
HP07	Tuffite/ Greyish black	40°46.457′N	118°36.971′E	236/38	8/11	0/8	291.2	-33.6	258.8	-59.3	71.4	6.6	-32.2	1.1
HP08	Andesite/Greyish red	40°49.342′N	118°38.860′E	238/32	8/11	0/8	252.5	-30.7	232.1	-32.9	114.4	5.2	-40.1	39.8
HP09	Andesite/Greyish red	40°49.365′N	118°38.846′E	238/32	10/10	0/10	262.7	-44.3	227.8	-48.7	116.2	4.5	-49.9	29.2
HP10	Andesite/Greyish red	40°49.394′N	118°38.827′E	238/32	8/10	0/8	286.2	-42.5	250.5	-59.7	61.8	7.1	-38.1	4.1
[b]HP11	Andesite/Greyish black	40°49.394′N	118°38.827′E	221/27	5/11	0/5	~~178.8~~	~~-63.0~~	~~157.2~~	~~-41.1~~	~~40.6~~	~~13.8~~	~~-64.2~~	~~173.3~~
[c]HP12	Andesite/Greyish black	40°51.772′N	118°40.176′E	5/54	8/10	8/0	~~4.0~~	~~63.5~~	~~63.0~~	~~32.0~~	~~43.4~~	~~8.5~~	~~31.5~~	~~212.5~~
HP13	Andesite/Greyish black	40°51.951′N	118°40.095′E	9/60	9/10	9/0	348.0	52.9	55.0	35.8	52.1	7.2	39.0	215.8
[c]HP14	Andesite/Greyish black	40°52.020′N	118°40.058′E	9/60	5/9	9/0	~~7.0~~	~~57.8~~	~~63.0~~	~~26.0~~	~~107.8~~	~~7.4~~	~~29.2~~	~~215.8~~
HP15	Tuffite/Purple red	40°57.942′N	118°51.766′E	351/35	5/11	0/5	151.9	-50.8	195.8	-48.9	105.0	7.5	-73.1	64.8
HP16	Tuffite/Purple red	40°57.942′N	118°51.766′E	351/35	7/8	0/7	153.1	-51.4	197.2	-48.6	98.9	6.1	-72.0	62.5
HP17	Tuff/Greyish green	40°57.780′N	118°52.117′E	15/40	8/10	8/0	348.0	53.7	46.0	52.1	78.2	6.3	52.7	206.5
HP18	Tuff/Greyish green	40°57.442′N	118°51.175′E	353/28	11/12	11/0	323.0	55.4	8.6	59.3	192.3	3.3	83.1	212.6
HP19	Tuff/Greyish red	40°56.453′N	118°51.368′E	302/15	13/13	13/0	12.0	72.7	21.0	58.3	275.7	2.5	73.8	208.8
HP20	Basalt/Greyish red	40°56.564′N	118°51.230′E	1/24	10/10	10/0	20.0	79.4	70.0	60.9	374.1	2.5	39.0	183.1
HP21	Basalt/Greyish red	40°55.206′N	118°47.595′E	323/6	5/11	0/5	207.9	-62.4	211.9	-56.8	148.4	6.3	-65.1	26.5
HP22	Tuff/Greyish red	40°55.224′N	118°47.340′E	323/6	10/10	0/10	192.2	-82.7	210.4	-77.5	720.5	1.8	-59.6	322.7
Sub-mean					**18/22**		**34.0**	**65.0**			**7.8**	**13.2**		

									38.4	**50.5**	**19.2**	**8.1**			
Kazuo and Jianchang, western Liaoning, Lanqi Formation															
LK01	Andesite/Greyish red	40°50.173′N	119°36.024′E	32/34	10/10	10/0	347.0	37.3	19.0	55.2	36.5	8.1	74.3	222.3
LK02	Andesite/Greyish red	40°50.319′N	119°34.746′E	21/30	7/9	7/0	357.0	31.1	18.0	38.6	117.1	5.6	65.6	255.5
LK03	Andesite/Greyish red	40°50.319′N	119°34.746′E	25/31	8/9	8/0	8.0	54.9	51.0	52.0	47.7	8.1	48.9	204.2
[a]LK04	Andesite/Greyish red	40°43.258′N	119°37.128′E	159/21	3/11	—	~~85.2~~	~~81.2~~	~~237.8~~	~~77.2~~	~~14.0~~	~~34.3~~	~~25.3~~	~~96.8~~
LK05	Tuff/ Greyish red	40°43.799′N	119°33.238′E	329/16	7/8	0/7	169.6	-79.3	211.5	-67.9	56.5	8.1	-66.1	353.9
LK06	Tuff Greyish red	40°43.799′N	119°33.238′E	329/16	9/11	0/9	232.5	-82.4	236.8	-66.8	88.6	5.5	-50.0	357.5
Sub-mean					**5/6**		**358.3**	**57.8**			**10.7**	**24.5**		
									33.0	**57.2**	**27.3**	**14.9**		
Mean for Pingquan, Kazuo and Jianchang					**23/28**		**24.5**	**64.2**			**8.1**	**11.3**	**59.6**	**208.8**
									37.4	**52.0**	**20.7**	**6.8**	**K=15.7**	**A_{95}=7.9**
Luanping, northern Hebei, Tiaojishan Formation (Ren et al., 2016)															
[a]LP01	Andesite	40°51.0′N	117°26.4′E	233/17	3/5	—	~~71.0~~	~~53.2~~	~~47.2~~	~~55.1~~	~~42.5~~	~~19.1~~	~~53.0~~	~~199.9~~
LP02	Andesite	40°51.0′N	117°26.4′E	233/17	9/9	—	85.4	63.8	47.5	68.0	135.5	4.4	56.1	173.6
LP03	Andesite	40°51.0′N	117°26.4′E	233/17	9/10	—	79.1	64.5	41.0	66.7	88.7	5.5	60.2	177.1
LP04	Andesite	40°51.0′N	117°26.4′E	233/17	8/8	—	78.7	61.8	44.7	64.5	31.0	10.1	57.6	182.4
LP05	Andesite	40°51.0′N	117°26.4′E	233/17	7/7	—	55.9	62.4	20.3	70.9	73.7	7.1	70.3	153.4
LP06	Andesite	40°51.0′N	117°26.4′E	233/17	6/6	—	11.1	70.9	349.7	57.1	84.8	7.3	81.4	9.2
LP08	Andesite	40°51.0′N	117°26.4′E	233/17	6/6	—	61.3	68.8	21.0	65.1	25.1	13.6	73.7	177.8
LP09	Andesite	40°51.0′N	117°26.4′E	233/17	4/4	—	52.7	66.5	18.9	61.2	57.0	12.3	75.8	195.4
LP10	Andesite	40°51.0′N	117°26.4′E	233/17	5/7	—	80.9	62.9	45.0	66.0	149.7	6.3	57.6	178.7
[a]LP11	Andesite	40°51.0′N	117°26.4′E	233/17	5/6	—	~~69.3~~	~~60.8~~	~~38.2~~	~~61.0~~	~~18.6~~	~~18.2~~	~~61.6~~	~~192.2~~
LP12	Andesite	40°51.0′N	117°26.4′E	233/17	6/8	—	80.1	67.6	35.8	69.2	71.9	8.0	63.1	168.9
LP13	Andesite	40°51.0′N	117°26.4′E	233/17	5/8	—	67.7	73.3	15.9	69.9	28.3	14.6	73.2	151.6
Beipiao, western Liaoning, Lanqi Formation (Ren et al., 2016)															

BP01	Andesite	41°48.6′N	120°36.0′E	253/34	5/8	—	264.3	-72.3	194.7	-55.4	136.6	6.6	-77.2	53.0
BP02	Andesite	41°48.6′N	120°36.0′E	253/34	9/10	—	279.5	-80.4	180.0	-59.2	100.4	5.2	-88.2	120.6
BP03	Andesite	41°48.6′N	120°36.0′E	253/34	4/7	—	282.8	-75.0	190.4	-60.8	158.0	6.1	-82.3	27.1
BP04	Andesite	41°48.6′N	120°36.0′E	253/34	9/10	—	295.1	-83.1	173.3	-60.2	96.4	5.3	-84.9	205.0
BP05	Andesite	41°48.6′N	120°36.0′E	253/34	5/6	—	277.0	-80.0	180.9	-58.9	235.4	5.0	-87.7	102.8
BP06	Andesite	41°48.6′N	120°36.0′E	253/34	6/7	—	268.1	-79.4	182.2	-57.3	200.3	4.7	-85.8	96.5
[d]BP07-11	Andesite	41°49.8′N	120°42.6′E	252/43	33/41	—	313.0	-54.3	219.5	-70.4	297.3	4.4	-61.3	350.8
Shouwangfen, northern Hebei, Tiaojishan Formation (Ren et al., 2016)														
SWF12	Andesite	40°35.88′N	117°45.6′E	341/42	5/5	—	345.4	60.9	32.7	38.7	68.5	9.3	56.6	232.0
SWF13	Andesite	40°35.88′N	117°45.6′E	341/42	8/8	—	291.0	73.6	49.9	60.4	23.8	11.6	52.9	189.7
SWF14	Andesite	40°35.88′N	117°45.6′E	341/42	8/8	—	338.0	72.6	45.5	46.1	21.2	12.3	50.6	212.7
Chengde, northern Hebei, Tiaojishan Formation (Pei et al., 2011)														
[a]CT38	Andesite	40°47.58′N	118°6.60′E	241/61	10/10	0/10	~~250.7~~	~~-39.7~~	~~207.8~~	~~-25.1~~	~~6.9~~	~~19.8~~	~~-53.2~~	~~68.8~~
CD3	Andesite	40°47.58′N	118°6.60′E	241/61	7/7	0/7	268.1	-52.2	195.4	-39.1	73.1	7.1	-67.2	78.6
CD4	Andesite	40°47.58′N	118°6.60′E	241/61	7/7	0/7	292.2	-50.9	192.9	-53.9	36.8	10.1	-78.0	55.9
CD5	Trachyandesite	40°47.58′N	118°6.60′E	241/61	8/8	0/8	272.0	-40.5	210.9	-41.1	24.9	11.3	-58.9	52.3
CD6-7	Trachyandesite	40°47.58′N	118°6.60′E	241/61	7/7	0/7	269.4	-45.6	205.4	-38.6	75.4	7.0	-61.3	62.0
CD8	Crystal tuff	40°47.82′N	118°6.42′E	241/61	5/5	0/5	267.3	-26.1	229.0	-32.5	76.2	8.8	-42.2	42.1
CD9-10	Crystal tuff	40°48.06′N	118°6.12′E	241/61	7/7	0/7	253.5	-42.2	205.8	-27.7	26.9	11.9	-55.6	69.9
CD12-13	Crystal tuff	40°48.06′N	118°6.12′E	241/61	7/8	7/0	94.7	44.8	26.6	42.4	79.0	6.8	62.5	236.2
CD14-15	Crystal tuff	40°48.12′N	118°5.61′E	241/61	8/8	7/1	86.3	44.5	25.2	37.3	51.2	7.8	60.8	243.5
Mean for the Tiaojishan and Lanqi formations					**51/59**		**54.9**	**68.0**			**9.3**	**6.9**	**66.1**	**208.3**
									30.6	**54.5**	**22.2**	**4.3**	**K=16.5**	**A_{95}=5.1**

1. Fold tests for the 23 sites from this study:
(1) Watson and Enkin's Test (2003): the optimal concentration is achieved at 106.9 ±4.8% unfolding level;
(2) McElhiny's Test (1964): N=23, *ks/kg*=2.56>F [44, 44]=1.65 indicative of a positive fold test at 95% confidence level;

(3) McFadden's Test (1990): N=23, in-situ ξ_2=13.28, tilt-corrected ξ_2=0.13, statistical threshold ξ=7.84 at 99% confidence level, indicative of a positive fold test.

2. Fold tests for the 51 sites combined from (Pei et al., 2011; Ren et al., 2016) and this study:

(1) Watson and Enkin's Test (2003): the optimal concentration is achieved at 80.2 ±3.7% unfolding level;

(2) McElhiny's Test (1964): N=51, *ks/kg*=2.39 > F [100, 100]=1.39 indicative of a positive fold test at 95% confidence level;

(3) McFadden's Test (1990): N=51, in-situ ξ_2=30.53, tilt-corrected ξ_2=17.64, statistical threshold ξ=11.76 at 99% confidence level, suggesting that the fold test is inconclusive.

3. Reversal test (McFadden and McElhinny, 1990):

(1) For the 23 sites from this study: the angular difference of 3.1 °between the normal and reversed polarities is less than the critical angle of 14.2 °indicative of a positive reversal test of C class.

(2) For the 51 sites combined from (Pei et al., 2011; Ren et al., 2016) and this study: the angular difference of 5.7 °between the normal and reversed polarities is less than the critical angle of 8.6 °indicative of a positive reversal test of B class.

4. Paleosecular variation (PSV) analysis (Deenen et al., 2011):

(1) For the 23 sites from this study: the Deenen's envelope for N=23 is 4.9 to 11.4 and the A_{95} of paleopole of the Tiaojishan/Lanqi formations is 7.9 suggesting that the PSV has been sampled out.

(2) For the 51 sites combined from (Pei et al., 2011; Ren et al., 2016) and this study: the Deenen's envelope for N=51 is 3.5 to 6.9 and the A_{95} for the Tiaojishan/Lanqi formations is 5.1 suggesting that the PSV has been sampled out.

5. PSV analysis (McFadden et al., 1991):

(1) For the 23 sites from this study: the calculated S is 20.5 and the acceptable S suggested by Model G is 16.5 to 21.1 suggesting that the PSV has been sampled out..

(2) For the 51 sites combined from (Pei et al., 2011; Ren et al., 2016) and this study: the calculated S is 19.9 and the acceptable S suggested by Model G is 16.5 to 21.1 suggesting that the PSV has been sampled out.

[a]Sites excluded for α_{95} larger than 15; [b]Sites excluded as outliers; [c]Sites excluded because the in-situ sites mean directions of which overlap the Earth's present magnetic field and a more scattered distribution is observed after the tilt correction when these sites are included; [d]Sites

combined for the tightly grouped directions at one location that were repeatedly sampled from the same layer of tuff. Other abbreviations are as for Table DR3.

Table DR5: Summary of paleomagnetic poles from NCB, Amuria during the Jurassic to Early Cretaceous.

Blocks	Locality	Lithology	Ages	Slat.	Slong.	N(P)	Plat.	Plong.	A_{95}(or dp/dm)	Reference
NCB+Amuria			120Ma			(5)	83.7	202.0	5.1	(Ren et al., 2018)
			130Ma			35	80.5	197.4	2.3	(Ren et al., 2018)
			140Ma			21	82.7	208.6	4.3	(Ren et al., 2018)
Amuria	Manzhouli	Volcanics	J_3	47.0	123.1	14	62.4	224.6	4.9	(Zhao et al., 1990)
	Hua'an	Volcanics	J_3	49.5	117.5	8	73.0	254.8	7.8	(Zhao et al., 1990)
	Southern Mongolia	Sandstones	J_3	44.5	109.2	16	74.7	232.5	3.7	(Zhao et al., 1990)
	Unda-Daya*	Volcanics	J_{2-3}	51.5	117.5	8	68.6	261.8	3.4/4.9	(Kravchinsky et al., 2002)
	Unda-Daya*	Volcanics	J_3	51.7	117.4	6	73.3	275.9	5.3/7.4	(Cogné et al., 2005)
NCB	Hebei and Liaoning	Andesite/Tuff	J_3(153-161Ma)	40.8	118.1	35	69.6	203.0	5.6	(Ren et al., 2016)
	Hebei	Andesite	J_3(153-161Ma)	40.8	118.1	9	59.9	240.3	6.8	(Pei et al., 2011)
	Hebei/Liaoning	Basalt/Tuff	J_3(153-161Ma)	40.9/40.8	118.6/119.5	23	59.6	208.8	7.9	**This study**
	Mean		J_3(153-161Ma)	41.0	119.0	51	66.1	208.3	5.1	(Pei et al., 2011; Ren et al., 2016 and this study)
	Hebei	Basalt/Tuff	J_{1-2}(168-180Ma)	42.1	117.9	25	65.9	140.3	9.1	**This study**

Abbreviations: Slat./Plat., the latitude of the sampling site /paleomagnetic pole, Slong./Plong., the longitude of sampling site/paleomagnetic pole; A_{95} is the radius of the 95% uncertainty circle for each pole, N(P) is the number of sites (paleomagnetic poles);
* Paleomagnetic poles calculated from *in-situ* ChRMs without constraints on the remagnetization age.

Table DR6: Jurassic to early Cretaceous APWPs for NCB and Eurasia.

Block/Continent	Age (Ma)	Plat.	Plong.	A_{95}
NCB+SCB (Van der Voo, et al., 2015)	100	80.8	152.3	3.3
	110	81.2	193.1	3.3
	120	78.0	162.5	4.1
	130	81.1	168.0	6.6
	150	72.3	177.0	5.1
	160	74.7	174.3	4.7
	170	78.0	160.7	9.6
	180	84.2	106	3.3
NCB (Huang et al., 2018)	120	81.5	214.1	7.6
	130	81.5	214.1	7.6
	150	68.8	224.5	15.9
	160	72.8	225.8	6.3
	170	75.8	227.2	7.2
	180	82.0	294.7	----
	190	82.0	294.7	----
Eurasia#(Kent and Irving, 2010; Kent et al., 2015)	100	81.5	177.6	4.4
	110	82.1	165.7	4.5
	120	78.6	198.8	2.7
	130	76.5	198.8	2.4
	140	70.1	209.2	6.8
	145	66.9	214.5	9.0
	156	79.5	185.4	2.8
	160	73.7	114.0	7.5
	170	71.1	112.0	6.5
	180	74.2	104.6	5.5

	190	73.5	99.5	6.7
	200	61.3	98.6	3.8
Eurasia (Torsvik et al., 2012)	100	77.6	163.2	14.3
	110	79.7	168.2	2.5
	120	78.7	179.0	--
	130	77.1	182.4	--
	140	75.3	181.7	2.9
	150	75.7	162.3	5.0
	160	72.9	138.0	5.7
	170	67.7	117.8	14.4
	180	68.5	107.2	6.6
	190	66.6	101.8	12.2
	200	57.7	99.7	10.9

Abbreviations are as for Table DR3.

GAPWaP (Kent and Irving, 2010; Kent et al., 2015) is rotated to Eurasia coordinates using rotation parameters from Kent and Irving (2010)

References

Brunet MF, et al. (2017) Late Paleozoic and Mesozoic evolution of the Amu Darya Basin. Geol Soc Lon, Spec Pub 427: 1-17.

Chu Z, et al. (2016) High-precision U-Pb geochronology of the Jurassic Yanliao biota from Jianching (western Liaoning Province, China): Age constraints on the rise of feathered dinosaurs and eutherian mammals. *Geochem Geophys Geosyst* 17: 3983-3992.

Cogné JP, Kravchinsky V, Halim N, Hankard F (2005) Late Jurassic-Early Cretaceous closure of the Mongol-Okhotsk Ocean demonstrated by new paleomagnetic results from the Trans-Baikal area (SE Siberia). *Geophys J Int* 163: 813-832.

Deenen MHL, et al. (2011) Geomagnetic secular variation and the statistics of paleomagnetic directions. *Geophys J Int* 186(2): 509-520.

Deng S, et al. (2017) Jurassic paleoclimatic zoning and evolution in China. Geosci Front 24: 106-142.

Dong F, Shih CK, Ren D (2014) Two new species of Trichoceridae from the Middle Jurassic Jiulongshan Formation of Inner Mongolia, China. *ZooKeys* 411: 145-160.

Fang D, et al. (1988) Tectonic implications of Triassic and Jurassic paleomagnetic results from Ningwu basin, Shanxi Province. *Chin Sci Bull* 33 (2): 133–135 (in Chinese).

Fang X, et al. (2016) Mesozoic litho- and magneto-stratigraphic evidence from the central Tibetan Plateau for megamonsoon evolution and potential evaporites. *Gond Res* 37: 110-129.

Fang Y, et al. (2015) Provenance of the southern Junggar Basin in the Jurassic: Evidence from detrital zircon geochronology and depositional environments. *Sedimentary Geol* 315: 47-63.

Fisher R (1953) Dispersion on a Sphere. *Proc Roy Soc Lond* 217: 295-305.

Gao HL, et al. (2018a) Ages of Jurassic volcano-sedimentary strata in the Yanshan Fold and Thrust Belt and their implications for the coal-bearing strata of northern China. *Int Geol Rev* 61: 956-971.

Gao HL, et al. (2018b) Wang, Dating Jurassic volcanic rocks in the western hills of Beijing, North China: implications for the initiation of the Yanshanian tectonism and subsequent thermal events. *J Asian Earth Sci* 161: 164-177.

Gilder S, Courtillot V (1997) Timing of the North‐South China collision from new middle to late Mesozoic paleomagnetic data from the North China block. *J Geophys Res* 102: 17713-17727.

Huang B, et al. (2018) Paleomagnetic constraints on the paleogeography of the East Asian blocks during Late Paleozoic and Early Mesozoic times. *Earth Sci Rev* 186: 8-36.

Huang D (2019) Jurassic integrative stratigraphy and timescale of China, *Sci China-Earth Sci* 62: 223-255.

Ji Q, Luo Z, Yuan C, Tabrum AR (2006) A swimming mammalian form from the Middle Jurassic and ecomorphological diversification of early mammals. *Science* 311: 1123-1127.

Kent DV, et al. (2015) Tracking the Late Jurassic apparent (or true) polar shift in U-Pb dated kimberlites from cratonic North America (Superior Province of Canada). *Geochem Geophys Geosyst* 16: 983-994.

Kent DV, Irving E (2010) Influence of inclination error in sedimentary rocks on the Triassic and Jurassic apparent polar wander path for North America an implications Cordilleran tectonics. *J Geophys Res* 115: B10103.

Kirschvink JL (1980) The Least-Squares Line and Plane and the Analysis of Paleomagnetic Data. *Geophys J Roy Astr Soc* 62: 699-718.

Kravchinsky, VA, Sorokin AA, Courtillot V (2002) Paleomagnetism of Paleozoic and Mesozoic sediments from the southern margin of Mongol-Okhotsk ocean, far eastern Russia. *J Geophys Res* 107.

Li Z, Dong S, Qu H (2014) Timing of the initiation of the Jurassic Yanshan movement on the North China Craton: evidence from sedimentary cycles, heavy minerals, geochemistry, and zircon U–Pb geochronology. *Int Geol Rev* 56: 288-312.

Lin C, Liu S, Zhuang Q, Steel RJ (2018) Sedimentation of Jurassic fan-delta wedges in the Xiahuayuan basin reflecting thrust-fault movements of the western Yanshan fold-and-thrust belt, China. *Sedimentary Geol* 368.

Liu Y, et al. (2010) Continental and Oceanic Crust Recycling-induced Melt–Peridotite Interactions in the Trans-North China Orogen: U–Pb Dating, Hf Isotopes and Trace Elements in Zircons from Mantle Xenoliths. *J Petrol* 51: 537-571.

Liu Y, Liu Y (2005) Comment on "$^{40}Ar/^{39}Ar$ dating of ignimbrite from Inner Mongolia, northeastern China indicates a post-middle Jurassic age for the overlying Daohugou bed" by H. Y. He et al. *Geophys Res Lett* 32: L12314.

Ludwig KR (2003) ISOPLOT 3.0: A geochronological toolkit for Microsoft Excel. Special, publication no. 4. Berkeley Geochronology Center.

Ma X, et al. (1993) Paleomagnetic study since late Paleozoic in the Ordos basin. *Acta Geophys Sin* 36

(1): 68–79.

Mattei M, Muttoni G, Cifelli F (2014) A record of the Jurassic massive plate shift from the Garedu Formation of central Iran. Geology 42: 555-558.

McElhinny MW (1964) Statistical significance of the fold test in paleomagnetism. *Geophys J Int* 8: 338-340.

McFadden PL (1990) A new fold test for paleomagnetic studies. *Geophys J Int* 103: 163-169.

McFadden PL, McElhinny MW (1990) Classification of the reversal test in paleomagnetism. *Geophys J Int* 103: 725-729.

McFadden PL, Merrill RT, McElhinny MW, Lee S (1991) Reversals of the earth's magnetic field and temporal variations of the dynamo families. *J Geophys Res* 96(B3): 3923-3933.

Pei J, et al. (2011) A paleomagnetic study from the Late Jurassic volcanics (155 Ma), North China: implications for the width of Mongol–Okhotsk ocean. *Tectonophys* 510: 370-380.

Ren Q, et al. (2016) Further paleomagnetic results from the ~ 155 Ma Tiaojishan Formation, Yanshan Belt, North China, and their implications for the tectonic evolution of the Mongol–Okhotsk suture. *Gond Res* 35: 180-191.

Ren Q, et al. (2018) New Late Jurassic to Early Cretaceous paleomagnetic results from North China and southern Mongolia and their implications for the evolution of the Mongol‐Okhotsk suture. *J Geophys Res* 123: 10370-10398.

Swisher C, et al. (2002) Further support for a Cretaceous age for the feathered-dinosaur beds of Liaoning, China:new $^{40}Ar/^{39}Ar$ dating of the Yixian and Tuchengzi formations. *Chin Sci Bull* 47(2): 135-138.

Tauxe L (2005) Inclination flattening and the geocentric axial dipole hypothesis. *Earth Planet Sci Lett* 233(3-4): 0-261.

Torsvik TH, et al. (2012) Phanerozoic polar wander, paleogeography and dynamics. *Earth Sci Rev* 114: 325-368.

Traynor JJ, Sladen C (1995) Tectonic and stratigraphic evolution of the Mongolian People's Republic and its influence on hydrocarbon geology and potential. *Marine Petrol Geol* 12: 35-52.

Uno K, & Huang B (2003) Constraints on the Jurassic swing of the apparent polar wander path for the North China Block. *Geophys J Int* 154: 801-810.

Van der Voo R, et al. (2015) Latest Jurassic–earliest Cretaceous closure of the Mongol-Okhotsk Ocean:

A paleomagnetic and seismological-tomographic analysis. *Geol Soc Am Spec Pap* 513: 589-606.

Wang S, Gao L (2012) SHRIMP U-Pb dating of zircons from tuff of Jurassic Qigu Formation in Junggar Basin, Xinjiang (in Chinese). *Geol Bull China* 31: 503–509.

Watson GS, Enkin RJ (2003) The fold test in paleomagnetism as a parameter estimation problem. *Geophys Res Lett* 20: 2135-2137.

Wiedenbeck M, et al. (1995) Three natural zircon standards for U-Th-Pb, Lu-Hf, trace element and REE analyses. *Geostan Geoanal Res* 19: 1–23.

Xu H, et al. (2012) U–Pb SHRIMP age for the Tuchengzi Formation, northern China, and its implications for biotic evolution during the Jurassic–Cretaceous transition. *Paleoworld* 21(3-4): 222-234.

Xu H, et al. (2013) Sedimentology, paleogeography and paleoecology of the Late Jurassic- Early Cretaceous aeolian sands in North China. *J Paleogeo* 15: 11-30.

Xu H, Liu YQ, Kuang HW, Peng N (2019) Late Jurassic fluvial-eolian deposits from the Tianchihe Formation, Ningwu-Jingle Basin, Shanxi Province, China. *J Asian Earth Sci* 174: 245-262.

Xu X, et al. (2008) Discovery of lias basalt northwestern edge of Junggar Basin and its geological significance (in Chinese). *Xinjiang Geol* 26: 9–16.

Yang ZY, et al. (1992) Jurassic paleomagnetic constraints on the collision of the North and South China Blocks. *Geophys Res Lett* 19 (6): 577–580.

Zhao X, et al. (1990) New paleomagnetic results from Northern China: collision and suturing with Siberia and Kazakhstan. *Tectonophys* 181: 43-81.

Zheng Z, et al. (1991) The apparent polar wander path for the North China Block since the Jurassic. *Geophys J Int* 104: 29-40.

Zijderveld JDA (1967) “Demagnetization of rocks: analysis of results” In Methods in paleomagnetism. pp. 254-286 (Elsevier).